2 ON THE CONSISTENCY OF HNO_3 AND NO_2 IN THE ALEUTIAN HIGH

3 REGION FROM THE NIMBUS 7 LIMS VERSION 6 DATASET

5 Ellis Remsberg[1], Murali Natarajan[1], and V. Lynn Harvey[2]

8 [1]Science Directorate, NASA Langley Research Center

9 21 Langley Blvd, Mail Stop 401B

10 Hampton, Virginia 23681, USA

12 [2]Laboratory for Atmospheric and Space Physics

13 Atmospheric and Oceanic Sciences

14 University of Colorado, UCB 311

15 Boulder, Colorado, 80309, USA

17 Correspondence to: Ellis Remsberg (ellis.e.remsberg@nasa.gov)

19   **Abstract.** This study uses photochemical calculations along kinematic trajectories in conjunction with

20   Limb Infrared Monitor of the Stratosphere (LIMS) observations to examine the changes in HNO_3 and

21   NO_2 near 30 hPa in the region of the Aleutian High (AH) during the minor warming event of January

22   1979. An earlier analysis of Version 5 (V5) LIMS data indicated increases in HNO_3 without a

23   corresponding decrease in NO_2 in that region and a wave-2 signature in the zonal distribution of HNO_3,

24   unlike the wave-1 signal in ozone and other tracers. Version 6 (V6) LIMS also shows an increase of

25   HNO_3 in that region, but NO_2 is smaller than from V5. The focus here is to convey that both V6

26   HNO_3 and NO_2 are of better quality than from V5, as shown here by a re-examination of their

27   mutual changes in the AH region. Photochemical model calculations initialized with LIMS V6 data

28   show increases of about 2 ppbv in HNO_3 over 10 days along trajectories terminating in the AH region on

29   28 January. Those increases are mainly a result of the nighttime heterogeneous conversion of N_2O_5 on

30   background stratospheric sulfuric acid aerosols. Changes in the composition of the air parcels depend on

31   the extent of exposure to sunlight and, hence, on the dynamically controlled history of the trajectories.

32   Trajectories that begin in low latitudes and traverse to across the Pole in a short time lead to the low

33   HNO_3 in the region separating the anticyclone from the polar vortex, both of which contain higher HNO_3.

34   These findings help to explain the observed seasonal evolution and areal extent of both species. V6

35   HNO_3 and NO_2 are suitable, within their errors, for the validation of stratospheric chemistry/climate

36   models.

1 Introduction and Objectives

The Limb Infrared Monitor of the Stratosphere (LIMS) experiment operated on Nimbus 7 from 25

October 1978 through 28 May 1979. LIMS measurements were originally processed and archived to a

Version 5 (V5) data set (see Gille and Russell, 1984, and references therein). Since then, the observed

LIMS radiance profiles have been re-processed with improved, Version 6 (V6) algorithms to provide

profiles of temperature, chemical species, and geopotential height, as a function of pressure-altitude from

65° S to 84° N latitude (Remsberg et al., 2004). There are improvements from the registration of the

LIMS radiance profiles and from updated spectroscopic line parameters for retrievals of the V6 species

profiles. Several studies already show that the V6 ozone is of better quality for scientific analysis

(Natarajan et al., 2002; Stolarski et al., 2013; Remsberg et al., 2013; Shepherd et al., 2014). The two

nitrogen species, nitric acid (HNO_3) and nitrogen dioxide (NO_2), are also of better quality in V6

(Remsberg et al., 2010). In particular, Holt et al. (2012) were able to quantify the exchange of V6 NO_2

from the mesosphere to the middle stratosphere within the polar vortex. Remsberg and Harvey (2016)

also found good relationships on the 550 K potential temperature surface (near 30 hPa) for the highest

values of V6 HNO_3, lowest values of ozone, and highest values of potential vorticity (PV) within the

Arctic winter vortex. While there are residual effects from polar stratospheric clouds (PSCs) in the ozone

and water vapor (H_2O), those effects are small in the HNO_3 and NO_2 profiles and occur only at

temperatures < 194 K and from about 1-20 January. The V6 data set is part of the SPARC Data Initiative

for chemistry-climate model comparison studies (Tegtmeier, et al., 2013; SPARC, 2017).

The northern hemisphere (NH) polar winter of 1978-1979 was dynamically active in the middle

stratosphere, as determined from daily surface plots of geopotential height (GPH), potential vorticity

(PV), and ozone on the 850 K potential temperature surface (near 10 hPa) (McIntyre and Palmer, 1983;

Leovy et al., 1985; Butchart and Remsberg, 1986). A major, zonal wave-1 forcing brought about a rapid

exchange of air between polar and middle latitudes from mid to late January. Rood et al. (1993)

64   (hereafter referred to as R93) analyzed the LIMS V5 data in the Aleutian High (hereafter referred to as

65   AH) region for 14-27 January. They reported that the tracer-like species HNO_3 on the 30-hPa surface

66   increased slowly during that time in the region of the relatively warm anticyclone. The absence in their

67   analysis of a corresponding decrease in NO_2 accompanying the increase in HNO_3 led to concerns of an

68   inconsistency in the LIMS data. The present study reconsiders that anomaly but using the V6 dataset and

69   a trajectory model that includes the chemistry of reactive nitrogen (NO_y) or the sum of HNO_3 and odd

70   nitrogen (NO_x).

71

72   In their analysis of the V5 data, R93 also noted finding high values of HNO_3 in both the polar vortex and

73   the AH, and lower values around the periphery of both circulation systems resulting in a zonal wave-2

74   signature in the HNO_3 distribution. They suggested that, since dynamically controlled species like ozone

75   showed a clear wave-1 signature similar to GPH and PV, the HNO_3 levels outside the polar vortex may

76   have influences from a mechanism independent of dynamics in order to account for its wave-2 variation.

77   They explored the possible role of heterogeneous chemistry on background sulfate aerosols in converting

78   NO_x to HNO_3 and concluded based on a 2-D model study that those species changes from V5 are large in

79   winter but not correct phenomenologically. Separate studies have shown that heterogeneous reactions

80   involving sulfate aerosols do perturb the stratospheric photochemistry and HNO_3 levels (Austin et al.,

81   1986; Rodriguez et al., 1991). With the availability of the improved V6 dataset, we revisit the question of

82   inconsistency for the LIMS HNO_3 and NO_2 observations in the AH region. We focus our attention on the

83   same period, namely 14 – 27 January, when there was a minor stratospheric warming.

84

85   Section 2 describes briefly the improvements implemented in the retrievals of the V6 profiles. We also

86   note that the unscreened, residual effects from unscreened PSCs in the polar vortex are small for HNO_3

87   relative to those in ozone. Section 3 contains polar plots of ozone, HNO_3, NO_2, and GPH for 17 and 27

88   January 1979 and describes their changes, as the AH develops and the center of the vortex moves off the

89   Pole. Section 4 shows the changes in V6 HNO_3 and NO_2 at the center of the AH from 14 to 27 January.

90   Section 5 describes an ensemble of trajectory calculations, including heterogeneous chemistry, for air

91   parcels converging in the region of the AH on 27 January. Those calculations partition NO_y into the

92   observed HNO_3 and NO_2, plus the unobserved variations of nitric oxide (NO) and nitrogen pentoxide

93   (N_2O_5). The calculated daily species values compare reasonably well with closest observed LIMS values,

94   as shown from the results in Section 6. We then show in Section 7 time series of variations of PV and of

95   V6 HNO_3, H_2O, and NO_2 on the 550 K potential temperature surface across most of the northern

96   hemisphere for the entire 7¼ months of LIMS data. In this way, the variations for January are set in the

97   context of the longer-term, seasonal changes for those species. Section 8 is a summary of the findings.

98

99   **2 Improvements of the LIMS V6 species**

100   The LIMS instrument obtained profiles of atmospheric limb radiance in six channels, a wide (W) and a

101   narrow (N) band channel for CO_2 (CO_2W and CO_2N) and one each for ozone, H_2O, HNO_3, and NO_2 (Gille

102   and Russell, 1984). Retrieved V6 profiles occur at a spacing of every 1.4° of latitude (~155 km) along the

103   orbit, although their horizontal, tangent-path resolution remains no better than about 320 km. Bandpass

104   filters (in cm^{-1}) for the LIMS instrument are CO_2W (579-755), CO_2N (637-673), ozone (926-1141), H_2O

105   (1370-1560), HNO_3 (844-917), and NO_2 (1560-1630) in terms of their 5 % relative response points. Both

106   the H_2O and NO_2 channels have an instantaneous field-of-view (IFOV) vertical width at the horizon of

107   3.6 km, while the other four channels have half that width or 1.8 km.

108

109   Retrievals of the V6 temperature and associated species profiles were obtained by using all successive,

110   up/down scan profile pairs along their observed, orbital tangent-path locations and at 18 levels per decade

111   of pressure-altitude, p(z), or spaced about every 0.88 km. The effective vertical resolution is the same

112   (~3.7 km) for the retrieved V6 temperature and for each of the species profiles (Remsberg et al., 2004),

113   such that one can evaluate better the combined changes of HNO_3 and NO_2 at a given pressure-level.

114   Further, the spectral line parameters used for the retrieval of the NO_2 were updated for the production of

115   V6, leading to values of nighttime NO_2 that are up to 20 % smaller than those of V5 in the upper and

116   middle stratosphere (Remsberg et al., 2010). An important addition to the V6 data set is the co-located

117   GPH for each of the retrieved profiles.

118

119   LIMS-retrieved ozone has a non-linear sensitivity to temperature and/or radiance biases and to the effects

120   of PSCs; retrieved H_2O mixing ratio is even more sensitive (Remsberg et al., 2007; 2009). On the other

121   hand, effects from PSCs are much less noticeable in HNO_3 and NO_2. As an example, Figure 1 shows the

122   relative effects for ozone and HNO_3 of the residual contamination or the unscreened effects of emission

123   from PSCs, plus the associated temperature and GPH on the 31.6-hPa surface for 11 January. Grid-point

124   data for the surface plots of Fig. 1 are from the V6 Level 3 zonal Fourier coefficient product (Remsberg

125   and Lingenfelser, 2010). The ozone panel of Fig. 1 shows values in the cold vortex region that are of the

126   order of 6 ppmv and not in keeping with the much lower surrounding values of 3 ppmv. White plus signs

127   indicate where there was a screening of profile segments perturbed by emissions from PSCs in ozone, and

128   the red dot indicates the presence of a PSC based on data from the Stratospheric Aerosol Monitor (SAM

129   II) experiment for comparison purposes. While there can be descent of ozone in the vortex from higher

130   altitudes, the excess ozone in the vortex region of Fig. 1 is due to the remaining, unscreened effects of the

131   PSCs. Note also that the PSC features occur only where the environmental temperature is less than about

132   194 K. Thus, effects of PSCs are minimal for most of the Arctic lower stratosphere, and they are not

133   present at all in the warmer AH region.

134

135   The lower right panel of Fig. 1 shows that HNO_3 also has values in the vortex that appear a bit high. Yet,

136   those values are nearly unaffected by the PSCs because the relationship between the observed LIMS

137   HNO_3 radiance and its retrieved mixing ratio is very nearly linear. In fact, simulation studies indicate that

138   a temperature bias error of 1 K has only a small, 3 % effect in the V6 HNO_3 mixing ratios from 10 to 50

139   hPa (Remsberg et al., 2010, their Table 1). Retrieved NO_2 also varies in a nearly linear way. Yet as with

140   ozone, there are no perturbing effects from PSCs for H_2O, HNO_3, or NO_2 in the AH region that is the

141   focus of the remainder of this study.

142

143   **3 LIMS V6 GPH, O_3, HNO_3, and NO_2 during January 1979**

144   R93 (and references therein) analyzed and presented results of GPH, ozone, and HNO_3 at 30 hPa from the

145   V5 data set for 14, 17, 23, and 27 January. They noted that ozone behaves as a tracer in terms of its

146   relation to changes in GPH and according to its associated transport fields. On the other hand, they found

147   that the HNO_3 distributions did not evolve in the same way, but developed a zonal wave-2 rather than

148   wave-1 character over a deep layer of the middle stratosphere (50 to 5 hPa). They also did not find clear

149   anti-correlations between the distributions of V5 HNO_3 and NO_2 in the more isolated AH region, at least

150   to the extent that the sum of those two gases do not change appreciably. We consider their variations

151   again using the V6 data.

152

153   Initially, Rood et al. (1987) had expressed some doubts about the accuracy of the Arctic GPH fields at 30

154   hPa from the operational meteorological analyses for January 1979. Figs. 2b and 3b are polar plots of the

155   zonal GPH anomalies (deviations from zonal mean) from V6 for the equivalent level of 31.6 hPa and for

156   two of the four days above, 17 and 27 January. Those GPH anomalies exhibit structures that are very

157   similar to those of R93 (their Figs. 1b and 1d). The large-scale flow is along the isolines of the GPH

158   anomalies or around the respective high and low centers. The AH strengthened significantly but

159   remained at about the same location from 17-27 January. Maximum ozone anomalies in Figs. 2a and 3a

160   are nearly coincident with the center of the AH, again in close agreement with the findings of R93 (their

161   Figs. 2b and 2d). There is strong meridional transport of air of relatively poor ozone along the western

162   edge of the AH to across the Pole from 17 to 27 January.

163

164   The large-scale, zonal anomalies in HNO_3 (Figures 2d and 3d) are opposite in sign to those of GPH and

165   ozone. One exception is the relatively low values of HNO_3 near 80° N, 0° E on 17 January in Fig. 2d,

166   which has been interpreted as due to an uptake of gas phase HNO_3 onto PSC particles just upwind a day

167   or so earlier (Remsberg and Harvey, 2016). Yet, by 27 January (Fig. 3d) the cyclonic circulation about

168   the low GPH center indicates clearly that there is net transport of low values of HNO_3 near 140° E, along

169   the axis of the polar night jet, across the Pole, and then to about 300° E. As a result, while both ozone and

170   NO_2 display the same zonal wave-1 structures as the GPH field on 27 January, the HNO_3 distribution

171   exhibits wave-2 structure. Figs. 2c and 3c represent NO_2 anomalies from profiles of just the LIMS V6

172   descending orbits, or from its nighttime values near 11:00 pm local time. Those anomalies for NO_2 are

173   from four zonal waves minus the zonal mean coefficient, rather than from six zonal waves as for all the

174   other LIMS Level 3 products. Most of the NO_x converts from NO to NO_2 at sunset, followed by a further,

175   partial conversion of the NO_2 to N_2O_5 up to the 11:00 pm observation time of LIMS (Brasseur and

176   Solomon, 2005). The respective panels of Figs. 2 and 3 demonstrate that ozone and NO_2 have large-scale

177   features of opposite sign in the AH region, while HNO_3 and NO_2 have anomaly patterns of the same sign.

178   Clearly, it is important to consider the amount of NO_x that is in the form N_2O_5 in the AH region during

179   that time.

180

181   Figure 4 shows the zonal variations from the V6 Level 3 coefficients for the latitude of 66° N on 27

182   January. HNO_3 within the polar vortex (0° to 90° E) is higher by nearly 2 ppbv compared to that in the

183   AH region (180° E to 240° E). Note from Fig. 3, however, that HNO_3 has a strong, positive Equator-to-

184   Pole gradient in the 0° to 90° E sector, whereas that of ozone is weak and slightly negative. Ozone in Fig.

185   4 has a broad, wave-1 character, while HNO_3 exhibits two minima (at 140° E and 300° E). At 10 hPa and

186   lower pressures (or at higher z) a wave-2 structure is no longer apparent in HNO_3. Variations of the

187   descending and ascending (daytime or ~1330 local time) NO_2 modes appear separately in Fig. 4. Diurnal

188   differences for NO_2 are only in the longitude sector from 60 to 120° E, or across the boundary of the cold

189   polar vortex and the warmer AH region. Relatively low ozone at this location results in only a slow

190   conversion of NO_2 at sunset to NO_3 and finally to N_2O_5. Consequently, a larger fraction of NO_x remains as

191   NO_2 at the time of the LIMS descending mode observations, or near 11:00 pm local time. The warmer

192   AH region from 180° E to 240° E, on the other hand, has higher ozone mixing ratio, and the decrease in

193   NO_2 from its maximum at sunset is steeper, bringing NO_2 mixing ratios at the time of the LIMS

194   descending mode observation close to the value of the ascending mode measurement. There is very little

195   diurnal difference in NO_2 in that longitude region. Thus, air parcel history is important for interpreting

196   observed changes in the distributions of these two reactive species even in the AH region.

197

198   **4 Changing composition within the Aleutian High**

199   Figure 5 shows variations in the V6 species from the Level 2 profiles at 31.6 hPa and at the center of the

200   AH, which is identified by the location of the maximum GPH anomaly. Note that Fig. 5, which is

201   analogous to Figure 7 of R93, also shows that the latitude of the AH moves poleward from about 60° N to

202   68˚ N from 14 to 27 January. Its longitude moves slightly, too, from 186˚ E on 14 January to 230˚ E on

203   19 January and then retreats partially to 214˚ E by 27 January. Red boxes in Figure 6 illustrate those

204   locations. GPH of the 31.6-hPa level at the center of AH grows from 23.0 to 23.8 km during that time.

205

206   Ozone and H_2O variations in Figure 5 are no greater than their estimated single profile uncertainties of

207   ~15 % at 30 hPa (Remsberg et al., 2007; 2009). They remain rather steady in the AH and are in keeping

208   with their small horizontal gradients on the 31.6-hPa surface and their relatively long chemical lifetimes.

209   HNO_3 shows significant change; it declines from 10 to 8.2 ppbv from 14 to 18 January, but then increases

210   rather steadily again to 10 ppbv by 27 January. Single profile uncertainty for HNO_3 is ~8 % at 30 hPa

211   (Remsberg et al., 2010). Descending (or late evening) NO_2 declines from 1.1 to 0.5 ppbv from 15 to 19

212   January, increases to about 1.0 ppbv on 23 January, before declining again to 0.4 ppbv on 27 January.

213   Ascending (early afternoon) NO_2 is smaller than descending NO_2 from 14 to 17 January, or when the AH

214   center is at about 60° N. As the AH central latitude shifts northward after 17 January, both the ascending

215   and descending NO_2 exhibit similar values and indicate that the daytime observations are from near to or

216   within the polar night boundary. Generally, the root-sum-squared (RSS) bias error for single NO_2 profiles

217   is ~30 % at this pressure level, although it may be a bit larger across the polar night boundary. In

218   particular, Remsberg et al. (2010, their Fig. 3) show an altitude-latitude plot of "zonal average NO_2" from

219   only the descending (11:00 pm) orbital segments of 15 January, when the polar vortex is still nearly

220   circular and centered on the Pole. Its vertical distribution at 60° N declines from 2.5 ppbv at 20 hPa to a

221   local minimum of < 1 ppbv at 35 hPa or about where HNO_3 also has its local maximum. In fact, the V6

222   retrieval algorithm sets NO_2 to zero, when the forward radiance for the tangent layer approaches the

223   measurement noise for that channel (5.5 x 10^{-4} w-m^{-2}-sr^{-1}). Thus, the effect of a finite (~3.7 km) vertical

224   resolution is to smooth across that local NO_2 minimum, giving a high bias in its final retrieved value.

225

226   **5 Trajectory model with photochemistry**

227   In this section, we examine the interplay between photochemistry and dynamics during the evolution of

228   HNO_3 in the AH by making use of photochemical calculations along trajectories that terminate in the AH

229   region on 27 January. In these calculations, we use the V6 level 2 profile data to initialize the air parcel

230   composition, which allows a comparison between model results and co-located observations along the

231   trajectory in the AH region. The trajectory model is driven by 3-dimensional meteorological data from

232   MERRA (Rienecker et al., 2011) corresponding to January 1979. This dataset includes 3-hourly

233   information on surface pressure, horizontal wind, vertical pressure velocity, and temperature on a 1.25°

234   longitude by 1.25° latitude grid. A family of 70 back trajectories is generated, with trajectories beginning

235   at 30 hPa from a grid of 2°-latitude by longitude covering a domain defined by 210° E and 218° E

236   longitudes and 60° N and 86° N latitudes. The starting time of the back trajectories is 09Z on 28 January,

237   which corresponds to a local time of 11:00 pm on 27 January at 210° E. This is close to the local time of

238   LIMS descending mode observations in this latitude region. The selected region overlaps the AH as seen

239   in the contour plot of V6 GPH anomalies for this day as shown in Fig. 3b. The model uses a 4th order

240   Runge-Kutta advection scheme to generate 3-dimensional, kinematic back trajectories. We save

241   trajectory parameters required for further calculations on an hourly basis.

242

243   Figure 6 shows the back trajectory beginning on 27 January at 214° E, 68° N and 30 hPa. The numbers in

244   black along the trajectory represent the day numbers. Red colored squares with day numbers represent

245   the history of the location of the AH center at 31.6 hPa based on the maximum V6 GPH anomaly. This

246   pressure level is the closest in LIMS data to 30 hPa. It is clear that between 22 and 27 January the

247   trajectory and the AH center remain in a region north of 54° N latitude, and the AH region provides an

248   isolated natural chemical laboratory for the constituents to evolve. Prior to 22 January the trajectory and

249   AH center diverge with the trajectory going backwards to latitudes as far south as 27° N. As we will

250   show later, the back trajectory beginning at 214° E and 60° N remains within the AH region or north of

251   45° N throughout the 10-day period. These differences among the trajectories affect their initial values

252   and the changes in air parcel composition.

253

254   Time-dependent photochemical calculations are conducted along the trajectories in the forward direction.

255   Information used in these calculations include the vertical ozone column along the trajectories based on

256   V6 Level 3 ozone data, background sulfate aerosol surface area densities for January 1979 adopted from

257   the IGAC/SPARC CCMI recommendations for Reference Simulation 1 (Eyring et al., 2013), and solar

258   zenith angle corresponding to the local time of day. Note that only a modest amount of aerosol surface

259   area is necessary for the heterogeneous mechanisms to occur (e.g., Austin et al., 1986). The starting

260   location and mixing ratios of measured species are determined by identifying for each trajectory the

261   spatially and temporally closest LIMS descending mode observation between 14 and 17 January.

262   Longitude separation between the trajectory and the V6 data is within 15°, latitude separation within 7.5°,

263   and time of measurement within an hour. We use an updated version of the stratospheric diurnal

264 photochemical model (Natarajan and Callis, 1997) to calculate the changes in the composition of the air

265 parcels until they reach the AH region on 27 January. Chemical kinetics data are adopted from the recent

266 JPL evaluation (Burkholder et al., 2015). Results from a time-dependent, 2-dimensional chemistry-

267 transport model (Callis et al., 1997) simulation corresponding to January 1979 provide initialization

268 estimates of other unmeasured HO_x, Cl_x, and NO_x species. The initialization procedure involves repeated

269 diurnal calculations at the fixed starting latitude, altitude, and day. During each diurnal cycle, the mixing

270 ratios of ozone, NO_2, and HNO_3 are set to the observed values at the local time of the LIMS descending

271 mode measurement (Natarajan et al., 2002). Within five diurnal cycles, the short-lived chemical species

272 reach near steady mixing ratios. Then, the photochemical model integration continues along each

273 trajectory until reaching the endpoint of 09Z on 28 January.

274

275 **6 Results and discussion**

276 We show in this section the results of sample trajectories that have behavior similar to those of the

277 ensemble and discuss the transformations occurring in the composition of the air parcels over their 10-day

278 transit. All trajectories terminate at 30 hPa but, since we use 3-dimensional kinematic trajectories based

279 on MERRA, there are fluctuations in pressure and altitude as the parcel moves along its trajectory. The

280 length of exposure to daylight also fluctuates and is not the same for all the trajectories. These

281 differences certainly affect the photochemical changes that occur.

282

283 Figure 7(a) shows, on a polar stereographic projection map of the Northern Hemisphere, three different

284 trajectories terminating at a longitude of 214° E. The latitude circles in the figure are 10° apart and

285 poleward of 20° N. The uppercase letters A, B, and C denote the starting location of the trajectories and

286 the lowercase letters a, b, and c mark the endpoints at 60° N, 72° N, and 80° N latitude, respectively. The

287 color scale ranging from 0 to 1 represents the accumulated hours of exposure to darkness along each

288 trajectory expressed as a fraction of the total length of the trajectory in hours. The cumulative fraction of

289   darkness at the endpoint is 0.70, 0.67, and 0.63 for the trajectories A-a, B-b, and C-c, respectively. Fig.

290   7(b) shows the same three trajectories but now color-coded to demonstrate the calculated variation of

291   HNO$_3$. Trajectory A-a starts at 222.1° E and 59.9° N on 17 January with an initial HNO$_3$ mixing ratio of

292   9.05 ppbv, adopted from the nearby LIMS observation. Both the starting and termination points for this

293   trajectory are very near the center of the AH as seen in the GPH anomaly contours (Fig. 3b). The mixing

294   ratio of HNO$_3$ increases to 10.8 ppbv, mostly due to the heterogeneous hydrolysis involving N$_2$O$_5$ and

295   sulfate aerosol. This conversion of NO$_x$ predominates while the parcel is in darkness.

296

297   Figure 8(a) shows the variation with time of selected chemical constituents as the air parcel moves along

298   trajectory A-a. Shown by the thick broken line at the top of the figure are the segments when the parcel

299   along this trajectory is in darkness. It is clear that HNO$_3$ increases during extended periods of darkness,

300   which occur more often when the parcel traverses through higher latitudes. This increase in HNO$_3$ comes

301   at the expense of other reactive nitrogen species as can be seen in the decrease in the mean value and

302   somewhat diminished amplitude of the diurnal variation of NO$_2$. There is also a dampening of the diurnal

303   variation of N$_2$O$_5$ because of limited exposure to sunlight, although its mean value remains higher. The

304   daytime peak mixing ratio of NO is low (not shown). When a trajectory is at lower latitudes (e.g.,

305   between 17 and 22 January), all NO$_x$ species display larger diurnal variations with little change in mean

306   value. HNO$_3$ also shows some diurnal fluctuations due to daytime photolysis followed by production due

307   to heterogeneous chemistry in darkness and with a slight overall increase in mean mixing ratio. After 22

308   January, the air parcel moves to higher latitudes and experiences extended periods of darkness, leading to

309   the steady increase in HNO$_3$. Thus, a combination of dynamics, which determines the trajectory that the

310   parcel follows, and both gas-phase and heterogeneous photochemistry explains the higher levels of HNO$_3$

311   measured by LIMS near 30 hPa in the AH region on 27 January. Ozone, which has a longer chemical

312   lifetime at this pressure level, shows almost no change. However, we also note that at lower pressures,

313   e.g., at 5 hPa, there is a similar impact of dynamics and photochemistry in the formation of pockets of low

314   ozone mixing ratio within the AH region during winter (Manney et al., 1995; Morris et al., 1998; Harvey

315   et al., 2004). The photochemical time constant for ozone at those pressure levels is short enough that air

316   parcels originating from lower latitudes and containing higher ozone go through a chemical

317   transformation, when confined for an extended period of time within the AH region. This results in a

318   destruction of ozone in reaching photochemical equilibrium under daylight conditions. Conversely, the

319   increase in HNO_3 at 30 hPa is due mainly to the nighttime heterogeneous chemistry.

320

321   In order to highlight the role of the heterogeneous reactions involving background sulfate aerosols, we

322   have repeated the photochemical calculations along the same trajectories but considering only gas-phase

323   reactions. Fig. 8(b) shows the mixing ratios in this case for trajectory A-a. HNO_3 decreases from the

324   initial mixing ratio of 9.1 ppbv and settles to a value closer to 8.0 ppbv by 20 January. Because we

325   initialized the parcel using LIMS HNO_3 data, that initial drop is indicative of the imbalance created by

326   removing the source due to heterogeneous conversion. Small diurnal fluctuations are apparent during the

327   passage through lower latitudes because of photolysis, but they are nearly absent when the parcel is in the

328   high latitude region. Without heterogeneous reactions, N_2O_5 remains the primary reservoir of NO_x during

329   the nighttime and reaches its peak values just when the parcel is about to emerge from darkness. The

330   mean mixing ratio of N_2O_5 is about 2 ppbv between 23 and 25 January, when the parcel experiences that

331   extended period of darkness at high latitude. The diurnal cycle for NO_2 exhibits larger amplitudes when

332   using only gas-phase reactions, since the absence of additional production of HNO_3 keeps the NO_x mixing

333   ratio higher. The difference in the mixing ratio of HNO_3 in the AH region between the two simulations

334   shows the impact of heterogeneous reactions in the partitioning of odd nitrogen. While the agreement for

335   HNO_3 between model and the LIMS data of Fig. 5 is good with the inclusion of heterogeneous reactions,

336   the comparison for NO_2 is worse; the model gives mixing ratios that are lower than the measurement.

337   Considine et al. (1992) also reached a similar conclusion in their 2-dimensional model study. But, that is

338 also when the V6 NO_2 in the AH region is near its local minimum of about 0.5 ppbv, and we noted in

339 Section 4 that such small retrieved values are likely to have a slight high bias.

340

341 Trajectory B-b, shown in Fig. 7(a), starts from 173.3° E and 23° N on 14 January. After spending a few

342 days in the lower latitudes, the air parcel along this trajectory takes a nearly meridional path to the AH

343 region. During the last 5 days the parcel remains confined in the AH region, similar to the parcel along

344 trajectory A-a. The chemical evolution along the trajectory, shown in Fig. 9(a), is also similar to that

345 along trajectory A-a displayed in Fig. 8(a). Large diurnal variations in NO_2 and N_2O_5 occur during the

346 initial period between 14 and 20 January, when the trajectory is in the lower latitudes. Even HNO_3

347 displays noticeable variations with an increase during night caused by the heterogeneous conversion of

348 N_2O_5 followed by a decrease due to photolysis during daytime. Amplitudes of the diurnal variations

349 diminish in the high latitude AH region, due to reduced photolytic loss, especially for HNO_3, during the

350 shorter daylight period and at higher zenith angles. The corresponding increase in the nighttime

351 heterogeneous conversion leads to HNO_3 mixing ratios greater than 10 ppbv at the end of the trajectory.

352 Between 22 to 25 January, NO_2 displays a steady diurnal cycle, while N_2O_5 shows a declining peak value.

353 The increase in HNO_3 does not occur with a corresponding decrease in NO_2. During extended periods of

354 darkness, NO_2 decreases to a negligible amount as shown at the end of the trajectory on 27 January.

355 When there are only gas phase reactions, the variation of HNO_3 is as shown by the red line. Again,

356 initialization of the photochemical model uses the V6 data, and the absence of heterogeneous reactions

357 introduces an imbalance leading to the negative tendency in HNO_3.

358

359 Trajectory C-c, shown in Fig. 7(a), starts from 79.9° E and 27.6° N on 17 January. Until 24 January, this

360 parcel stays south of 40° N and then takes a meridional path directly northward reaching 80° N by 28

361 January. This is slightly north of the AH but still outside the polar vortex. Fig. 9(b) shows variations of

362 the species mixing ratios along the trajectory C-c for the simulation with heterogeneous chemistry. The

363   HNO$_3$ mixing ratio at the beginning of the trajectory (C) is about 7.8 ppbv, and it increases to about 8.7

364   ppbv at the endpoint (c). The measurements in Fig. 3(d) indicate a wave-2 feature in HNO$_3$ at 30 hPa,

365   with peak values in the polar vortex region and AH. The minimum in HNO$_3$ between these two regions is

366   a result of the rapid transit of air parcels from lower latitude along trajectories similar to C-c. The air

367   parcels remain in the low latitudes for a longer time, and photolysis during daylight hours keeps the net

368   change in HNO$_3$ low. Only later is there a noticeable increase in HNO$_3$ for the high latitude segment of

369   the trajectory. NO$_2$ and N$_2$O$_5$ display diurnal variations as expected in the middle latitudes. After 21

370   January, there is a decrease occurring in the peak value of NO$_2$ at every successive sunset along the

371   trajectory. The corresponding minimum in N$_2$O$_5$ shows a small increasing trend especially after 24

372   January, and this is due to the increasing lifetime against photolysis at winter high latitudes. The parcel is

373   in complete darkness during the last 24 hours, when NO$_2$ continuously decreases to a very low mixing

374   ratio, N$_2$O$_5$ declines slowly, and HNO$_3$ increases.

375

376   Calculated HNO$_3$ mixing ratios are shown in Figure 10 on a longitude-latitude grid for the end time of the

377   ensemble of 70 trajectories, corresponding to 09Z on 28 January. The latitudinal variation in HNO$_3$

378   between 60° N in the AH region and the Pole clearly shows a dip to lower values near 80° N in the model

379   calculations. This spatial distribution occurs even when heterogeneous reactions are not included.

380   However, calculations with heterogeneous chemistry simulate the magnitude of the LIMS HNO$_3$

381   observations better. Combined with the higher HNO$_3$ values in the polar vortex (not a focus of this

382   paper), the differing trajectories explain the formation of a wave-2 like structure at 30 hPa seen in the

383   LIMS HNO$_3$ observations during the minor warming. As reported by R93, this feature is present in the

384   LIMS V5 data also, except that V5 HNO$_3$ is nearly of the same magnitude in the AH and the polar vortex

385   at 30 hPa on 27 January. For the same conditions, the V6 HNO$_3$ is larger in the polar vortex than in the

386   AH by about 2 ppbv.

387

388   Even though we have shown and discussed the model results for only three of the trajectories, all of

389   which end along 214° E longitude, the results for the entire ensemble provide a consistent picture. A

390   scatter plot of the calculated HNO_3 along the 70 trajectories versus the spatially and temporally closest

391   LIMS observation is shown in Figure 11a. There is little bias between the model and LIMS data, except

392   for mixing ratios greater than 10 ppbv where the model values are higher. A similar scatter plot for NO_2

393   is displayed in Figure 11b, where values from the model are lower than the V6 observations. Deviations

394   from the diagonal dashed line for both HNO_3 and NO_2 could be due to a variety of factors, in addition to

395   bias errors of the data. The criteria we used for selecting the closest observation are coarse, but tightening

396   those criteria reduces the amount of data available for initializing the model and for comparison along the

397   trajectory. While we used the closest LIMS observation to constrain the initialization of the model, other

398   unmeasured species as well as total odd nitrogen are from two-dimensional model output that introduces

399   some uncertainty. We have used the recommended kinetic rate constants, but any uncertainty in key

400   reaction rates could affect the calculated variations in the composition. Another possible source of error

401   is the background stratospheric aerosol, surface area density. We have used the climatology from

402   IGAC/SPARC CCMI database, which are zonally averaged data. There were no major volcanic

403   perturbations in late 1978 and early 1979, so large perturbations from this database are most unlikely.

404   While at the lower latitudes photolysis during the daylight hours is important in limiting the impact of

405   heterogeneous reactions, the aerosol data directly affects that rate of conversion of N_2O_5 to HNO_3. It may

406   be that background aerosols in the vortex at high latitudes are less abundant than prescribed, which could

407   explain the apparent high bias in model HNO_3 for values greater than 10 ppbv in Figure 11a. Although

408   LIMS did not measure N_2O_5, analyses involving ATMOS measurements show clearly the role of N_2O_5

409   and heterogeneous reactions in the stratospheric odd nitrogen chemistry (Natarajan and Callis, 1991). A

410   more comprehensive study of the changes in atmospheric composition in the AH region using data from

411   more recent satellite experiments is beyond the scope of this study.

412

7 Seasonal evolution of PV, HNO$_3$, H$_2$O, and NO$_2$

413

414 Anticyclone features usually develop in the Northern Pacific stratosphere and are present 60 % of the time

415 during winter (Harvey and Hitchman, 1996; Baldwin and Holton, 1988). Therefore, we place the V6

416 species variations of 14-27 January into the broader context of their seasonal variations. As before, one

417 can ignore the effects of any remnants from PSCs for the species away from the polar winter vortex.

418 First, Figure 12 is a time series plot of the dynamical tracer, PV, on the isentropic surface of 550 K (near

419 31.6 hPa) for 25 October 1978 through 28 May 1979.

420 $$PV = (f + \zeta) / \sigma , \tag{1}$$

421 where $f = 2\Omega \sin \phi$ is the local vertical component of the planetary vorticity on a pressure surface and $\zeta =$

422 $(r \cos \phi)^{-1} (\partial v/\partial \lambda - \partial(u \cos \phi)/\partial \phi)$ is the relative vorticity in polar coordinates (longitude λ and latitude

423 ϕ). σ is isentropic density (kg m^{-2} K^{-1}) and $1/\sigma = -g \, \partial\theta/\partial p = (1/\varrho) \, \partial\theta/\partial z$ is static stability. Geostrophic

424 wind components, u and v, are calculated at grid points from the V6 GPH fields. Then, daily values of

425 the vertical component of PV are computed at each grid point from the zonal and meridional components

426 of the wind (u and v), plus the local vertical gradients of potential temperature versus pressure from V6,

427 following Harvey et al. (2009). The ordinate of Fig. 12 is in terms of equivalent latitude ϕ from the Pole

428 (90°) to 15° N and is from a monotonic ordering of the daily PV from high values inside the polar vortex

429 to lower values outside (see e.g., Butchart and Remsberg, 1986). Thus, equivalent latitude is a vortex-

430 centered coordinate that assigns the highest PV values (located in the center of the vortex) to be at 90° N.

431 Tic marks along the abscissa denote the middle of each month, and the PV time series have a seven point

432 smoothing. The ordinate is linear in ϕ to accentuate variations in the PV field at high equivalent latitudes.

433 The effects of the AH on the displacement and erosion of the PV vortex during 14-27 January are in Fig.

434 12 from ϕ of about -60° to 90° and following the tic mark labeled 01.

435

436   The effect of the AH in peeling away material contours from the edge of polar vortex has been described

437   aptly (e.g., McIntyre, 1995; Juckes and McIntyre, 1987; Rose, 1986). Fig. 12 indicates the continual

438   erosion of highest PV values during late winter and early spring due to zonal planetary wave-1 (the AH)

439   and wave-2 activity. The adjacent "surf zone" region of lower PV values expands and exhibits weakened

440   gradients ($\phi \sim 30°$ to $60°$) from the meridional mixing of PV across both the lower and higher latitudes

441   (McIntyre and Palmer, 1983). It is also noted that the vortex was split (wave-2) at four separate times at

442   the level of 31.6 hPa: late October, late November/early December, late February, and in early April.

443   Both scales of zonal forcing are indicative of the effects of planetary wave activity as it propagates from

444   the troposphere to the 31.6-hPa level (Juckes and O'Neill, 1988). The meridional gradient of PV is quite

445   weak equatorward of $\phi \sim 60°$ N in winter and then across all latitudes by mid-April, or after the polar

446   vortex has undergone significant erosion. The large-scale anticyclones and associated zonal easterlies

447   expand toward the middle latitudes by April.

448

449   The corresponding HNO_3 distribution is shown in Figure 13, as determined by averaging its values

450   around the daily PV contours and ordered according to the ϕ of Fig. 12. Those averages represent

451   approximate, modified Lagrangian mean (MLM) values for HNO_3 or its average values around the PV

452   contours, and they enable one to identify differences in behavior (e.g., chemical changes) for trace

453   constituents versus PV (McIntyre, 1980; Butchart and Remsberg, 1986). HNO_3 varies nearly

454   monotonically with latitude at this level, and values as high as 12 ppbv are found near the center of the

455   vortex ($\phi = 90°$) by late November and during the polar night. Such high values indicate a nearly

456   complete chemical conversion of the available NO_y to its reservoir species HNO_3. Poleward of about $\phi = $

457    $70°$ the HNO_3 contours are aligned well with those of PV, indicating that HNO_3 is an excellent tracer at

458   550 K, particularly in winter polar night when further chemical changes are inefficient.

459

460   A sequence of polar orthographic plots (not shown) indicates that there is a buildup of HNO_3 inside the

461   polar vortex in November, punctuated by meridional transport during the zonal wave-1 events of early

462   December and in January, and then followed by a splitting of the vortex in mid to late February. There is

463   significant transport of HNO_3 from the polar region to middle latitudes ($\phi = 45$ to $20°$) during those

464   events. Meridional gradients of HNO_3 are larger in winter at both ϕ of $70°$ and near $20°$, marking the

465   polar and subtropical edges of the region of efficient meridional mixing. The subtropical boundary of the

466   so-called "tropical pipe" region shifts from $\phi = 25°$ to about $15°$ from early December to late January and

467   then remains at that location into springtime (Remsberg and Bhatt, 1996). There is erosion of the high

468   HNO_3 values of the polar vortex by early March. Thereafter, HNO_3 decreases at all equivalent latitudes,

469   due to the daily effects of the chemical re-partitioning of NO_y away from HNO_3 and toward NO and NO_2

470   during sunlight.

471

472   Figure 14 displays the time series plot of the MLM for V6 H_2O, a better tracer of stratospheric transport.

473   Relatively large values of 5.5 to 6.0 ppmv occur at high latitudes from mid-November to early January

474   and indicate the effects of the slow descent of higher values within the vortex. H_2O is higher in the upper

475   stratosphere from the oxidation of methane. Elevated H_2O values at $\phi > 75°$ on 13-15 and 19 January are

476   due to residual emissions from PSCs. However, values ~7 ppmv also appear in early February to mid-

477   March, when temperatures are much too warm for the existence of PSCs. Although those higher values

478   are within the uncertainties for retrieved H_2O, they compare well with times when there is a descent of

479   higher ozone values in response to the major stratospheric warmings (c.f., Fig. 18 in Leovy et al., 1985).

480

481   Finally, the MLM plot of V6 NO_2 is given in Figure 15, based on only its profiles along descending

482   (nighttime) orbital segments. Smallest values of NO_2 occur in the polar vortex in late November and

483   early December, when the HNO_3 values of Fig. 13 reach 13 ppbv. As with H_2O, there are several minor

484   increases in NO_2 at the highest latitudes in mid-January; they occur at locations of residual effects from

485   PSCs. The excess values of NO_2 poleward of $\phi = 75°$ in February occur where the variations of PV

486   shown in Fig. 12 also indicate the effects of transport and where there may have been descent of higher

487   NO_2 values within the vortex (Holt et al., 2012). The distribution of NO_2 away from the vortex varies

488   more slowly and smoothly.

489

490   There are significant seasonal variations of NO_2 displayed in Fig. 15 at middle equivalent latitudes.

491   Conversion of NO_y to HNO_3 occurs in the presence of background aerosols from late autumn to winter,

492   followed by photochemical conversion of the HNO_3 vapor back to NO_2 in springtime (e.g., Austin et al.,

493   1986). Fig. 15 shows that the very low values of NO_2 extend from near the Pole to at least $\phi = 30°$ in

494   early December, and then retreating toward higher latitudes by late February. This variation of the NO_2

495   time series is an indicator of the so-called "Noxon cliff" feature of stratospheric column NO_2 during

496   winter (e.g., Noxon, 1979). Fig. 12 also indicates that there is considerable mixing for PV at $\phi \sim 60°$ to

497   75° during February, and Fig. 15 shows that NO_2 is increasing along the PV contours. The vortex split

498   into two sectors in the middle stratosphere from mid to late February, when there was transport and

499   descent of air having higher NO_2 values at the high latitudes. NO_2 increases steadily from March to May,

500   due to the conversion of HNO_3 to NO_2 upon the return of sunlight.

501

502   **8 Conclusions**

503   A significant improvement of the LIMS V6 data set is the better accuracy of its retrieved NO_2 profiles,

504   particularly away from the cold winter vortex region. Both the V6 HNO_3 and NO_2 are of good quality, at

505   least to within their respective error estimates and away from very cold regions of the vortex and their

506   PSC remnants. The V6 data are evaluated further in terms of the consistency of the HNO_3 and NO_2

507   distributions in the AH region during the minor warming event that took place in January 1979. In an

508   earlier analysis of the LIMS V5 data, R93 had highlighted an increase in HNO_3 at 30 hPa but with little

509   change in NO_2 within the AH region and suggested the need for some unknown process leading to the

510   production of HNO_3 and to the development of the wave-2 signature in its zonal distribution. This study

511   considered photochemical model calculations along kinematic trajectories over a 10-day period that

512   terminate in the AH region on 28 January. They indicate that there was an increase of about 2 ppbv in

513   HNO_3 and a decrease of order 0.5 ppbv in NO_2, mainly as a result of heterogeneous reactions converting

514   N_2O_5 on surfaces of background stratospheric sulfuric acid aerosols. R93 alluded to this mechanism but

515   reported that their two- and three-dimensional model studies with heterogeneous chemistry gave results

516   that did not agree so well with the observations from LIMS V5. The latitudinal variations of HNO_3 at the

517   end of our Lagrangian trajectory calculations agree better with LIMS V6. Those variations depend on the

518   initial conditions and the extent of exposure of air parcels to sunlit and dark conditions, and hence on the

519   dynamically controlled history of the different trajectories. Our model results show the formation of the

520   dip in observed HNO_3 mixing ratios north of the AH, due to meridional transport of low latitude air across

521   the Pole. Therefore, we conclude that the approaches and methods of R93 and Considine et al. (1992)

522   were valid and should have led to reasonable comparisons if the V6 data were available.

523

524   The inclusion of heterogeneous reactions improves the model comparisons for both HNO_3 and NO_2. The

525   model still underestimates NO_2 for some trajectories compared to the V6 values, however. A part of

526   those differences may be due to an inability to retrieve a local minimum in the V6 NO_2 profile with good

527   accuracy, at least based on the finite field of view of NO_2 channel radiances and their associated LIMS

528   temperature profiles. Still, the present study demonstrates that a combination of dynamical and

529   photochemical changes will explain the maximum mixing ratios of HNO_3 in both the AH region and at

530   the winter polar vortex, with lower values around the periphery of both circulation systems. When the

531   effects of heterogeneous chemistry are included, the calculated variations of HNO_3 and NO_2 along

532   trajectories agree more reasonably with the LIMS observations in the relatively isolated AH region.

533 HNO$_3$ re-partitions by photochemistry toward NO$_2$ during springtime, when the anticyclone regions

534 extend to middle latitudes. The observed evolution of HNO$_3$ and NO$_2$ during 1978-1979 is a separate

535 aspect of the V6 data for a validation of chemistry/climate models in the middle to lower stratosphere.

536

537 **Acknowledgements.** The V6 data set is archived at the Goddard Earth Sciences Data and Information

538 Services Center (GES DISC and its Website: daac.gsfc.nasa.gov) and is accessible for scientific use via

539 ftp download.

540

541   **References**

542   Austin, J. A., Garcia, R. R., Russell III, J. M., Solomon, S., and Tuck, A. F.: On the atmospheric

543   photochemistry of nitric acid, J. Geophys. Res., 91, 5477-5485, 1986.

544

545   Baldwin, M. P., and Holton, J. R.: Climatology of the stratospheric polar vortex and planetary

546   wave breaking, J. Atmos. Sci., 45, 1123-1142, 1988.

547

548   Brasseur, G. P. and Solomon, S.: Aeronomy of the middle atmosphere, 3rd Edition, Springer, The

549   Netherlands, 644 pp., 2005.

550

551   Burkholder, J. B., Sander, S. P., Abbatt, J., Barker, J. R., Huie, R. E., Kolb, C. E., Kurylo, M. J.,

552   Orkin, V. L., Wilmouth, D. M., and Wine, P. H.: Chemical kinetics and photochemical data for

553   use in atmospheric studies, Evaluation No. 18, JPL Publication 15-10, Jet Propulsion Laboratory,

554   Pasadena, 2015, http://jpldataeval.jpl.nasa.gov.

555

556   Butchart, N. and Remsberg, E. E.: The area of the stratospheric polar vortex as a diagnostic for

557   tracer transport on an isentropic surface, J. Atmos. Sci., 43, 1319-1339, 1986.

558

559   Callis, L. B., Natarajan, M., Lambeth, J. D., and Boughner, R. E.: On the Origin of Midlatitude

560   Ozone Changes: Data Analysis and Simulations for 1979 -1993, J. Geophys. Res., 102, 1215-

561   1228, 1997.

562

563   Considine, D. B., Douglass, A. R., and Stolarski, R. S.: Heterogeneous conversion of N_2O_5 to

564   HNO_3 on background stratospheric aerosols: comparisons of model results with data, Geophys.

565   Res. Lett., 19, 397-400, 1992.

566

567   Eyring, V., Lamarque, J.-F., Hess, P., Arfeuille, F., Bowman, K., Chipperfield, M. P., Duncan,

568   B., Fiore, A., Gettelman, A., Giorgetta, M. A., Granier, C., Hegglin, M., Kinnison, D., Kunze,

569   M., Langematz, U., Luo, B., Martin, R., Matthes, K., Newman, P. A., Peter, T., Robock, A.,

570   Ryerson, T., Saiz-Lopez, A., Salawitch, R., Schultz, M., Shepherd, T. G., Shindell, D., Staehelin,

571   J., Tegtmeier, S., Thomason, L., Tilmes, S., Vernier, J.-P., Waugh, D. W., and Young, P. J.:

572   Overview of IGAC/SPARC chemistry-climate model initiative (CCMI) community simulations

573   in support of upcoming ozone and climate assessments, SPARC Newsletter No. 40, January,

574   2013.

575

576   Gille, J. C. and Russell III, J. M.: The limb infrared monitor of the stratosphere: experiment

577   description, performance, and results, J. Geophys. Res., 89, 5125-5140, 1984.

578

579   Harvey, V. L. and Hitchman, M. H.: A climatology of the Aleutian High, J. Atmos. Sci., 53,

580   2088-2101, 1996.

581

582   Harvey, V. L., Pierce, R. B., Hitchman, M. H., Randall, C. E., and Fairlie, T. D.: On the

583   distribution of ozone in stratospheric anticyclones, J. Geophys. Res., 109, D24308,

584   doi:10.1029/2004JD004992, 2004.

585

586 Harvey, V. L., Randall, C. E., and Hitchman, M. H.: Breakdown of potential vorticity-based

587 equivalent latitude as a vortex-centered coordinate in the polar winter mesosphere, J. Geophys.

588 Res., 114, D22105, doi:10.1029/2009JD012681, 2009.

589

590 Holt, L. A., Randall, C. E., Harvey, V. L., Remsberg, E. E., Stiller, G. P., Funke, B., Bernath, P.

591 F., and Walker, K. A.: Atmospheric effects of energetic particle precipitation in the Arctic winter

592 1978-1979 revisited, J. Geophys. Res., 117, D05315, doi:10.1029/2011JD016663, 2012.

593

594 Juckes, M. N., and McIntyre, M. E.: A high-resolution one-layer model of breading planetary

595 waves in the stratosphere, Nature, 328, 590-596, 1987.

596

597 Juckes, M. N., and O'Neill, A.: Early winter in the northern stratosphere, Quart. J. R. Meteorol.

598 Soc., 114, 1111-1125, 10.1002/qj.49711448211, 1988.

599

600 Leovy, C. B., Sun, C.R., Hitchman, M. H., Remsberg, E. E., Russell III, J. M., Gordley, L. L.,

601 Gille, J. C., and Lyjak, L. V.: Transport of ozone in the middle stratosphere: evidence for

602 planetary wave breaking, J. Atmos. Sci., 42, 230-244, 1985.

603

604 Manney, G. L., Froidevaux, L., Waters, J. W., Zurek, R. W., Gille, J. C., Kumer, J. B.,

605 Mergenthaler, J. L., Roche, A. E., O'Neill, A., and Swinbank, R.: Formation of low-ozone

606 pockets in the middle stratospheric anticyclone during winter, J. Geophys. Res., 100, D7, 13,939-

607 13,950, 1995.

608

609   McIntyre, M. E.: Towards a Lagrangian-mean description of stratospheric circulations and

610   chemical transport, Phil. Trans. R. Soc. London, A296, 129-148, 1980.

611

612   McIntyre, M. E.: The stratospheric polar vortex and sub-vortex: fluid dynamics and midlatitude

613   ozone loss, Phil. Trans. R. Soc. London, A352, 227-240, 1995.

614

615   McIntyre, M. E. and Palmer, T. N.: Breaking planetary waves in the stratosphere, Nature, 305,

616   593-600, 1983.

617

618   Morris, G. A., Kawa, S. R., Douglass, A. R., Schoeberl, M. R., Froidevaux, L., and Waters, J.:

619   Low-ozone pockets explained, J. Geophys. Res., 103, D3, 3599-3610, 1998.

620

621   Natarajan, M. and Callis, L. B.: Stratospheric photochemical studies with Atmospheric Trace

622   Molecule Spectroscopy (ATMOS) measurements, J. Geophys. Res., 96, D5, 9361-9370,

623   doi:10.1029/91JD00290, 1991.

624

625   Natarajan, M. and Callis, L. B.: Ozone variability in the high latitude summer stratosphere,

626   Geophys. Res. Lett., 24, no. 10, 1191-1194, 1997.

627

628   Natarajan, M., Remsberg, E. E., and Gordley, L. L.: Ozone budget in the upper stratosphere:

629   model studies using the reprocessed LIMS and the HALOE datasets, Geophys. Res. Lett., 29, no.

630   7, doi:10.1029/2001GL014262, 2002.

631

632   Noxon, J.: Stratospheric NO_2, 2. global behavior, J. Geophys. Res., 84, no. C8, 5067-5076, 1979.

633

634   Remsberg, E. E., and Bhatt, P. P.: Zonal variance of nitric acid vapor as an indicator of

635   meridional mixing in the subtropical lower stratosphere, J. Geophys. Res., 101, 29,523-29,530,

636   1996.

637

638   Remsberg, E. and Harvey, V. L.: Effects of polar stratospheric clouds in the Nimbus 7 LIMS

639   Version 6 data set, Atmos. Meas. Tech., 9, 2927-2946, doi:10.5194/amt-9-2927-2016, 2016.

640

641   Remsberg, E. and Lingenfelser, G.: LIMS Version 6 Level 3 dataset, NASA/TM-2010-216690,

642   available at http://www.sti.nasa.gov (last access: 6 May 2015), 13 pp., 2010.

643

644   Remsberg, E. E., Gordley, L. L., Marshall, B. T., Thompson, R. E., Burton, J., Bhatt, P., Harvey,

645   L. V., Lingenfelser, G., and Natarajan, M.: The Nimbus 7 LIMS version 6 radiance conditioning

646   and temperature retrieval methods and results, J. Quant. Spectros. Rad. Transf., 86, 395-424,

647   doi:10.1016/j.jqsrt.2003.12.007, 2004.

648

649   Remsberg, E., Lingenfelser, G., Natarajan, M., Gordley, L., Marshall, B. T., and Thompson, E.:

650   On the quality of the Nimbus 7 LIMS version 6 ozone for studies of the middle atmosphere, J.

651   Quant. Spectros. Rad. Transf., 105, 492-518, doi:10.1016/j.jqsrt.2006.12.005, 2007.

652

653   Remsberg, E. E., Natarajan, M., Lingenfelser, G. S., Thompson, R. E., Marshall, B. T., and

654   Gordley, L. L.: On the quality of the Nimbus 7 LIMS Version 6 water vapor profiles and

655   distributions, Atmos. Chem. Phys., 9, 9155-9167, https://doi.org/10.5194/acp-9-9155-2009,

656   2009.

657

658   Remsberg, E., Natarajan, M., Marshall, B. T., Gordley, L. L., Thompson, R. E., and

659   Lingenfelser, G.: Improvements in the profiles and distributions of nitric acid and nitrogen

660   dioxide with the LIMS version 6 dataset, Atmos. Chem. Phys., 10, 4741-4756, doi:10.5194/acp-

661   10-4741-2010, 2010.

662

663   Remsberg, E., Natarajan, M., Fairlie, T. D., Wargan, K., Pawson, S., Coy, L., Lingenfelser, G.,

664   and Kim, G.: On the inclusion of Limb Infrared Monitor of the Stratosphere version 6 ozone in a

665   data assimilation system, J. Geophys. Res., 118, 7982-8000, doi:10.1002/jgrd.50566, 2013.

666

667   Rienecker, M.M., Suarez, M. J., Gelaro, R., Todling, R., Bacmeister, J., Liu, E., Bosilovich, M.

668   G., Schubert, S. D., Takacs, L., Kim, G.-K., Bloom, S., Chen, J., Collins, D., Conaty, A., da

669   Silva, A., Wei G., Joiner, J. , Koster R. D., Lucchesi, R., Molod, A., Owens, T., Pawson, S.,

670   Pegion, P., Redder, C. R., Reichle, R., Robertson, F. R., Ruddick, A. G., Sienkiewicz, M., and

671   Woollen, J.: MERRA: NASA's Modern-Era Retrospective Analysis for Research and

672   Applications. J. Climate, 24, 3624-3648, doi:10.1175/JCLI-D-11-00015.1, 2011.

673

674   Rodriguez, J. M., Ko, M. K. W., and Sze, N. D.: Role of heterogeneous conversion of N_2O_5 on

675   sulfate aerosols in global ozone losses, Nature, 352, 134-137, doi:10.1038/352134a0, 1991.

676

677   Rood, R. B., Kaye, J. A., Nielsen, J. E., Schoeberl, M. R., and Geller, M. A.: Nitric acid forecast

678   experiments, Physica Scripta, 36, 337-354, 1987.

679

680   Rood, R. B., Douglass, A. R., Kaye, J. A., and Considine, D. B.: Characteristics of wintertime

681   and autumn nitric acid chemistry as defined by limb infrared monitor of the stratosphere (LIMS)

682   data, J. Geophys. Res., 98, 18,533-18,545, 1993.

683

684   Rose, K.: The stratospheric winter polar vortex simulated as a material entity, J. Atmos. Terr.

685   Phys., 48, 1197-1202, 1986.

686

687   SPARC: The SPARC Data Initiative: Assessment of stratospheric trace gas and aerosol

688   climatologies from satellite limb sounders. M. I. Hegglin and S. Tegtmeier (Eds.), SPARC

689   Report No. 8, WCRP-05/2017, doi:10.3929/ethz-a-010863911, available at www.sparc-

690   climate.org/publications/sparc-reports/, 2017.

691

692   Stolarski, R. S., Douglass, A. R., Remsberg, E. E., Livesey, N. J., and Gille, J. C.: Ozone

693   temperature correlations in the upper stratosphere as a measure of chlorine content, J. Geophys.

694   Res., 117, D10305, doi:10.1029/2012JD017456, 2012.

695

696   Shepherd, T. G., Plummer, D. A., Scinocca, J. F., Hegglin, M. I., Fioletov, V. E., Reader, M. C.,

697   Remsberg, E., von Clarmann, T., and Wang, H. J.: Reconcilation of halogen-induced ozone loss

698   with the total-column ozone record, Nature Geoscience, 7, 443–449, doi:10.1038/ngeo2155,

699   2014.

700

701   Tegtmeier, S., Hegglin, M. I., Anderson, J., Bourassa, A., Brohede, S., Degenstein, D.,

702   Froidevaux, L., Fuller, R., Funke, B., Gille, J., Jones, A., Kasai, Y., Krüger, K., Kyrölä, E.,

703   Lingenfelser, G., Lumpe, J., Nardi, B., Neu, J., Pendlebury, D., Remsberg, E., Rozanov, A.,

704   Smith, L., Toohey, M., Urban, J., von Clarmann, T., Walker, K. A., Wang, R. H. J.: SPARC

705   Data Initiative: A comparison of ozone climatologies from international satellite limb sounders,

706   J. Geophys. Res., 118, 12,229–12,247, doi:10.1002/2013JD019877, 2013.

707

708
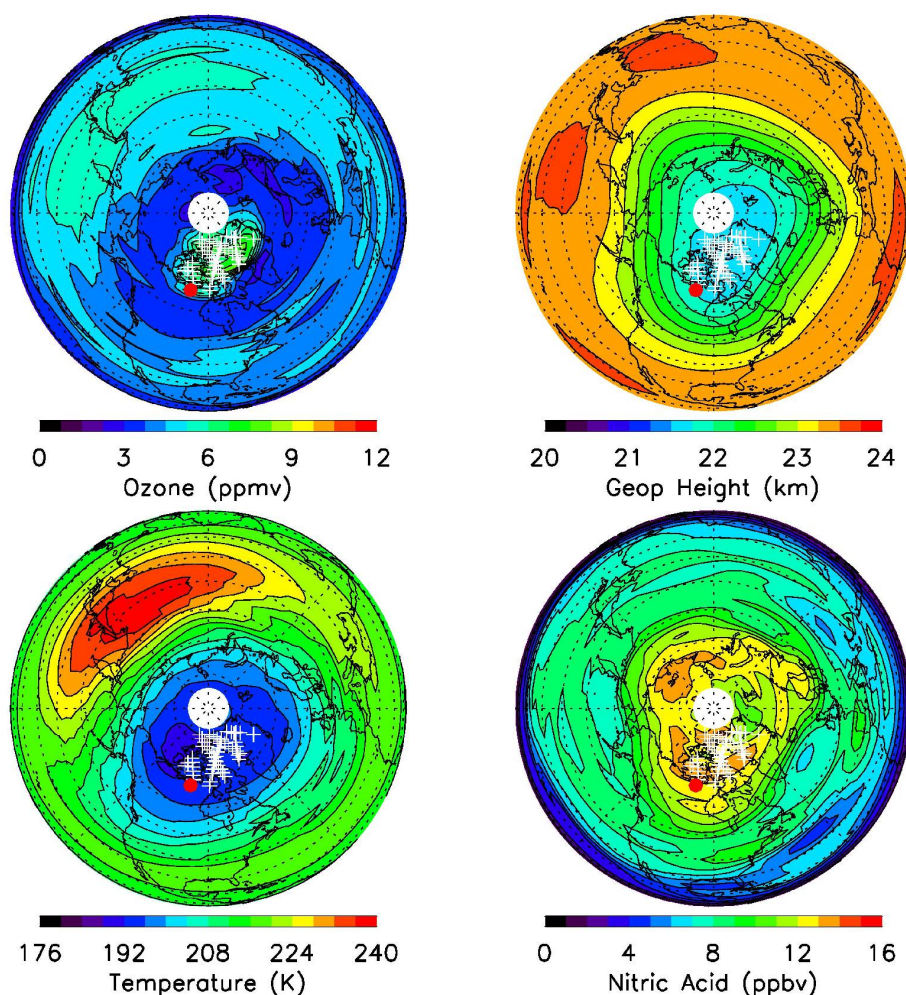
709

Figure 1. Polar orthographic projections of Northern Hemisphere ozone (top left), geopotential

height (GPH, top right), temperature (bottom left), and gas phase nitric (bottom right) for 11

January 1979 at 31.6 hPa; successive latitude circles are at every 10˚. The Greenwich meridian

extends horizontally to the right. Contour intervals are every 0.75 ppmv for ozone, 0.25 km for

GPH, 4 K for temperature, and 1 ppbv for nitric acid. White plus signs denote orbital profile

segments that are missing; red dot denotes location of a SAM II PSC observation.

716

717

718
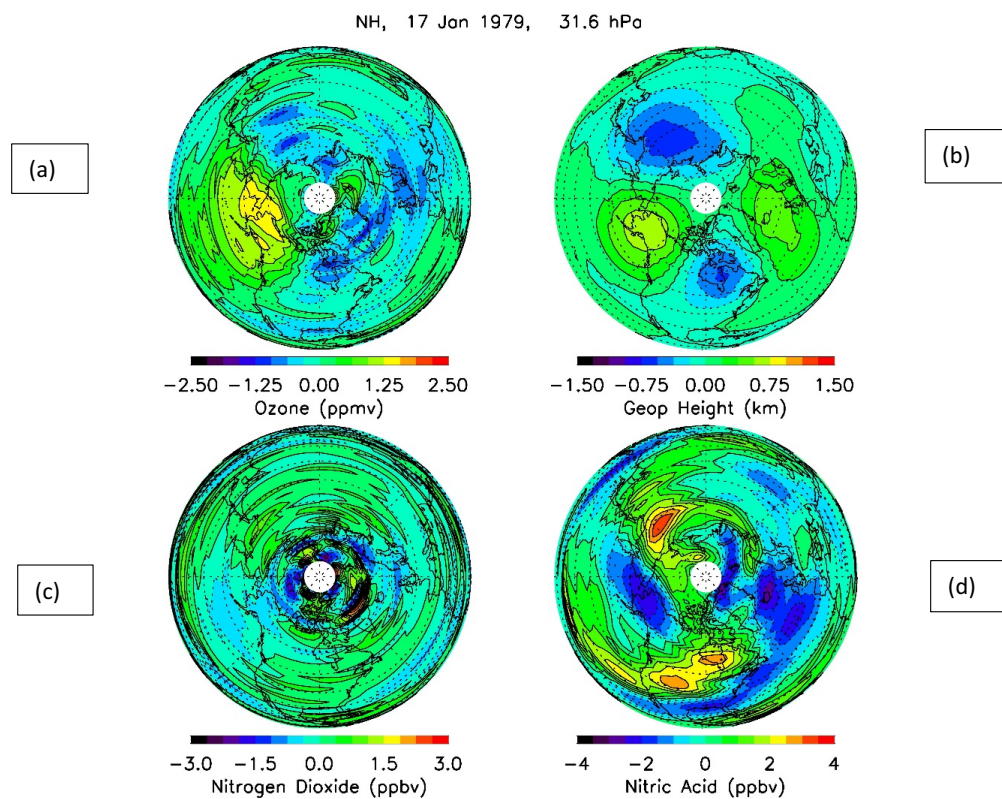
Figure 2. Zonal anomalies of ozone, GPH, nitrogen dioxide, and nitric acid for 31.6 hPa on 17
January 1979.

721

722

723

724
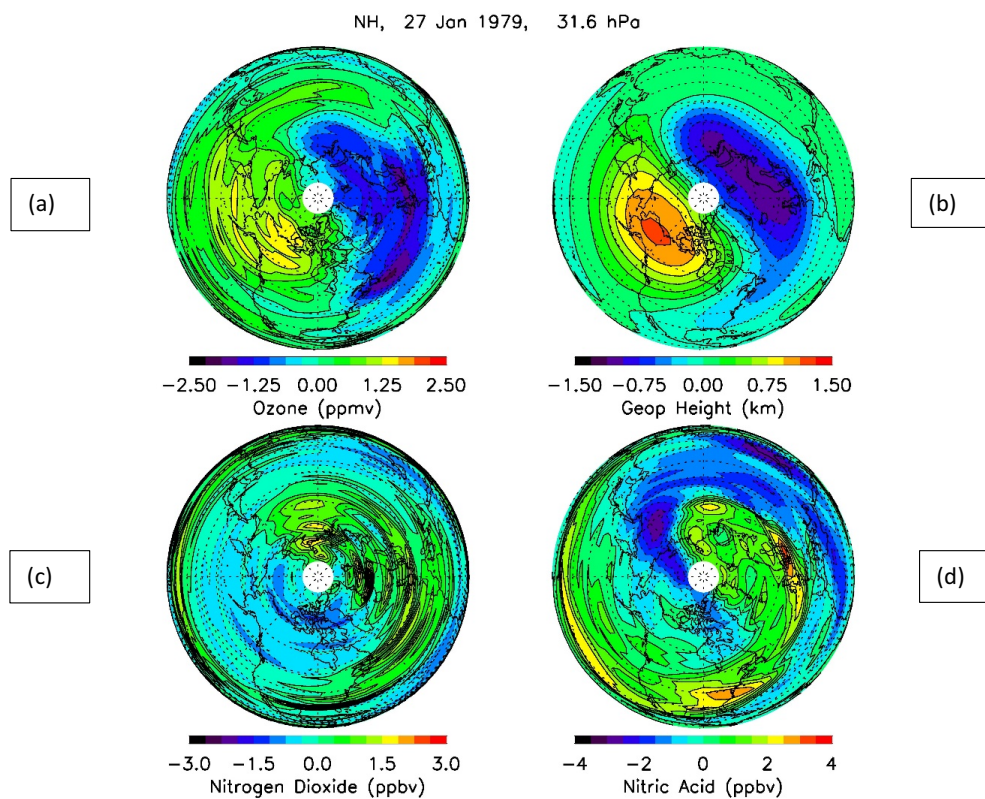
Figure 3. As in Fig. 2, but for 27 January 1979.

726

727
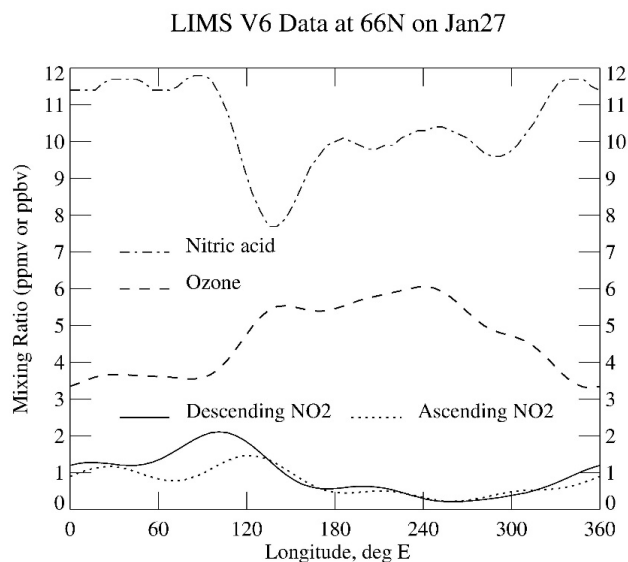
Figure 4. Zonal variations of LIMS species at 66˚ N on 27 January 1979. Vortex is between 0

and 90° E and AH region is from 180 and 240° E.

730

731
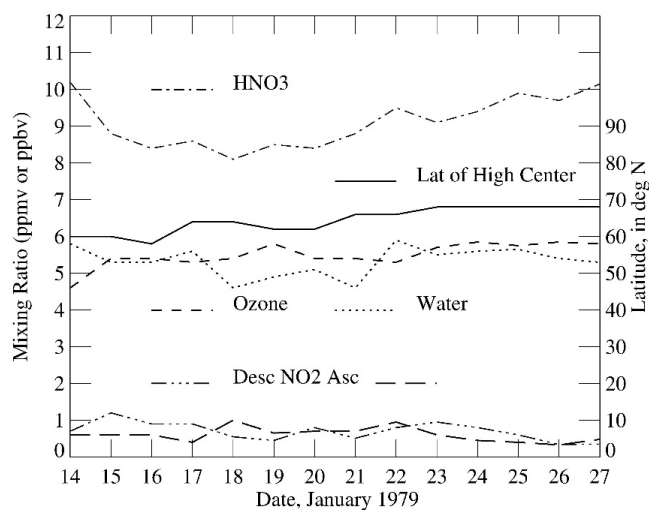
732

733   **Figure 5.** Time series of observed LIMS V6 species at 31.6 hPa and at the center of the Aleutian

734   High anomaly; its latitude is the solid curve.

735

736
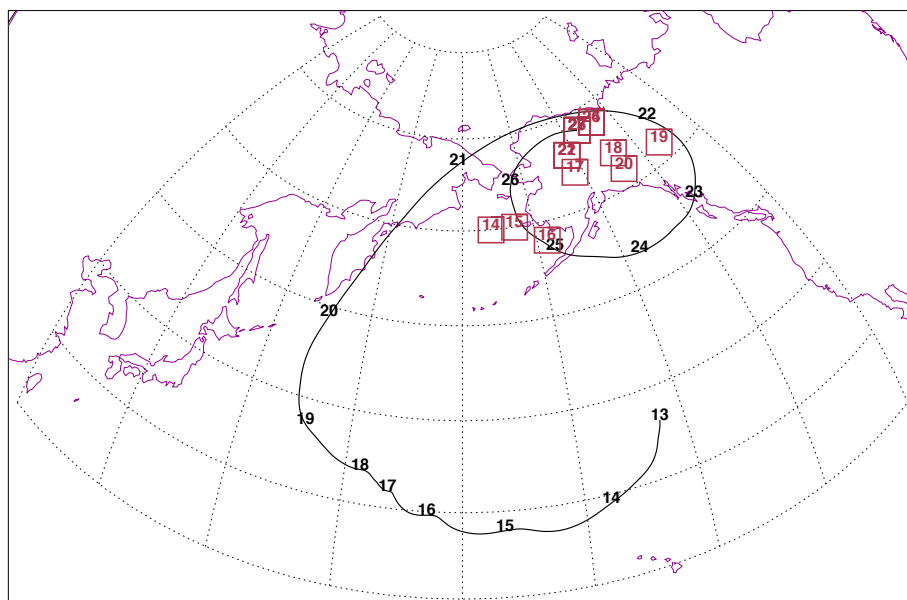
737

Figure 6. History of the location of maximum GPH anomaly at 31.6 hPa representing the AH center and displayed by red squares with day numbers. Latitude spacing is 10° beginning at 20° N and longitude spacing is 15° beginning at 120° E. Note that between 21 and 27 January the AH center occupies the same location on different days. The location on 27 January is 214° E and 68°N. Black line with day numbers describes the back trajectory beginning at 214° E, 68° N, and 30 hPa.

744

745

(a)
(b)
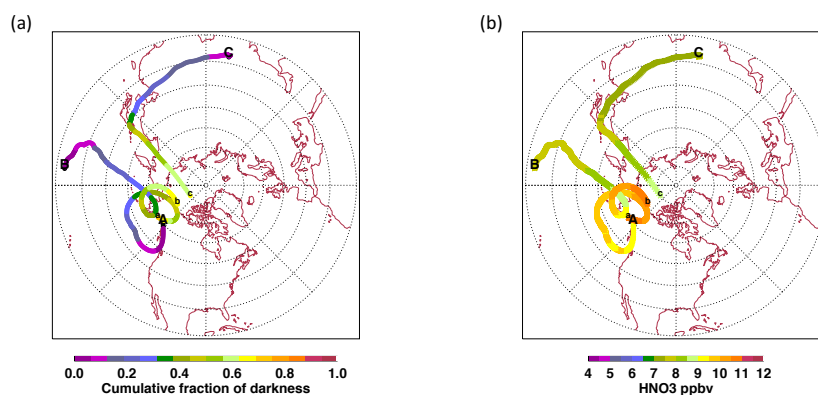
746
747
748   **Figure 7.** (a) Back trajectories beginning at 11:00 pm on 27 January (9Z on January 28) from 30

749   hPa, 214° E, and three different latitudes **[a]** 60° N, **[b]** 72° N, and **[c]** 80° N. The corresponding

750   endpoints **A, B,** and **C** are spatially and temporally closest to LIMS descending mode

751   measurement locations between 14 and 17 January. The latitude grids are 10° apart, starting

752   from 20° N and the Prime meridian extends horizontally to the right. The color scale refers to

753   the accumulated hours of darkness expressed as a fraction of the total length of the trajectory in

754   hours as the air parcel moves in the forward direction starting from locations **A, B,** and **C** and

755   ending at **a, b,** or **c** along 214° E longitude. (b) Evolution of HNO$_3$ along the three trajectories

756   shown in the left panel.

757

758
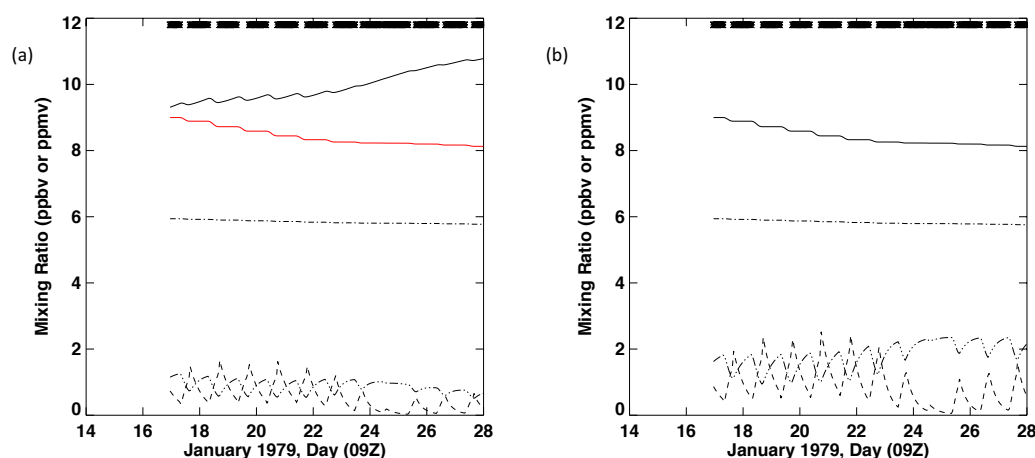
759

760

761 **Figure 8.** Mixing ratio of selected species as a function of time along the trajectory A-a shown

762 in Figure 7a. Air parcel terminates at 214° E and 60° N. HNO_3 (solid), NO_2 (dash), and N_2O_5

763 (dash-dot-dot) are in ppbv, and ozone (dash-dot) is in ppmv. The tick marks on the abscissa

764 correspond to 09Z hours on the dates shown. The thick line at the top represents the periods of

765 darkness along the trajectory with intermittent gaps corresponding to sunlit segments. (a)

766 Results from the case including heterogeneous reactions. (b) Results from the case with only gas

767 phase reactions.

768

769

770

771
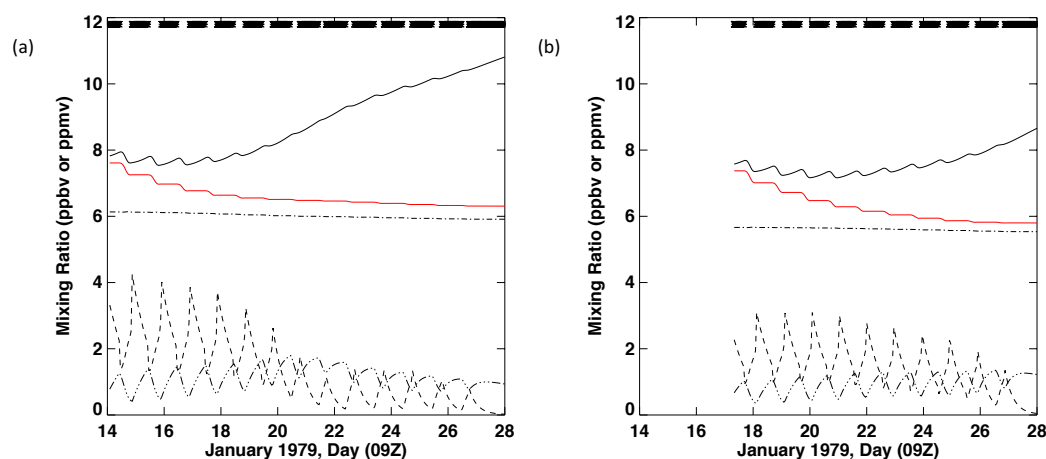
Figure 9. Mixing ratio of selected species as a function of time for the case with heterogeneous reactions as shown in Figure 8(a) but for trajectory B-b (a) and trajectory C-c (b). HNO_3 (solid), NO_2 (dash), and N_2O_5 (dash-dot-dot) are in ppbv, and ozone (dash-dot) is in ppmv. The red line in both panels represent the HNO_3 variation for the case with only gas phase reactions.

776

777

778

779
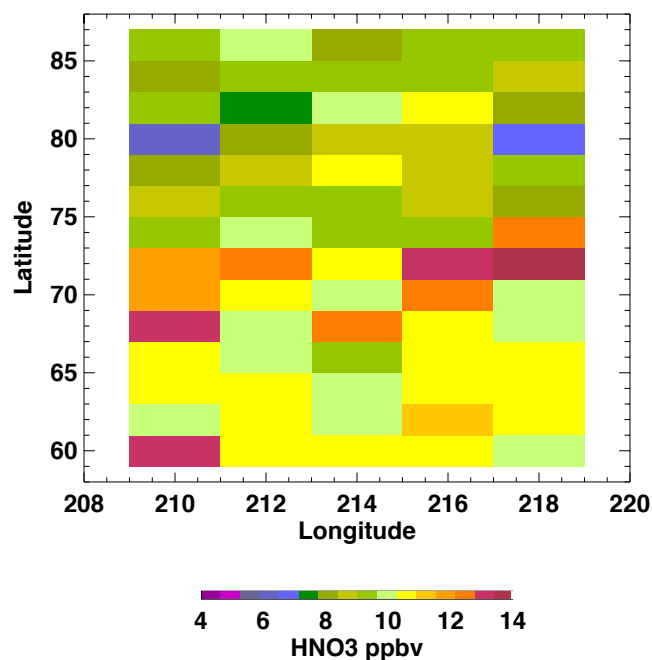
Figure 10. Calculated HNO$_3$ at 09Z on 28 January, corresponding to terminal location of all 70 trajectories.

782

783
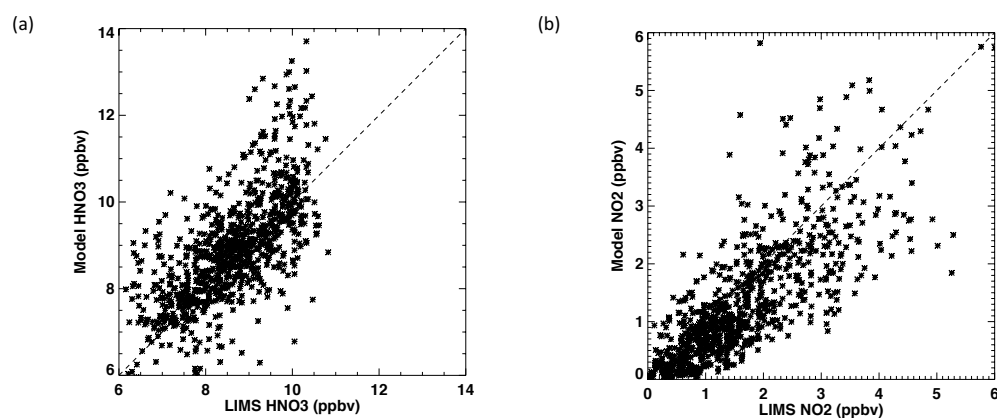
784

785

786 **Figure 11.** Scatter plot of calculated species mixing ratios along the 70 trajectories and of the

787 corresponding spatially and temporally closest LIMS observation. (a) HNO_3; (b) NO_2.

788
789

790
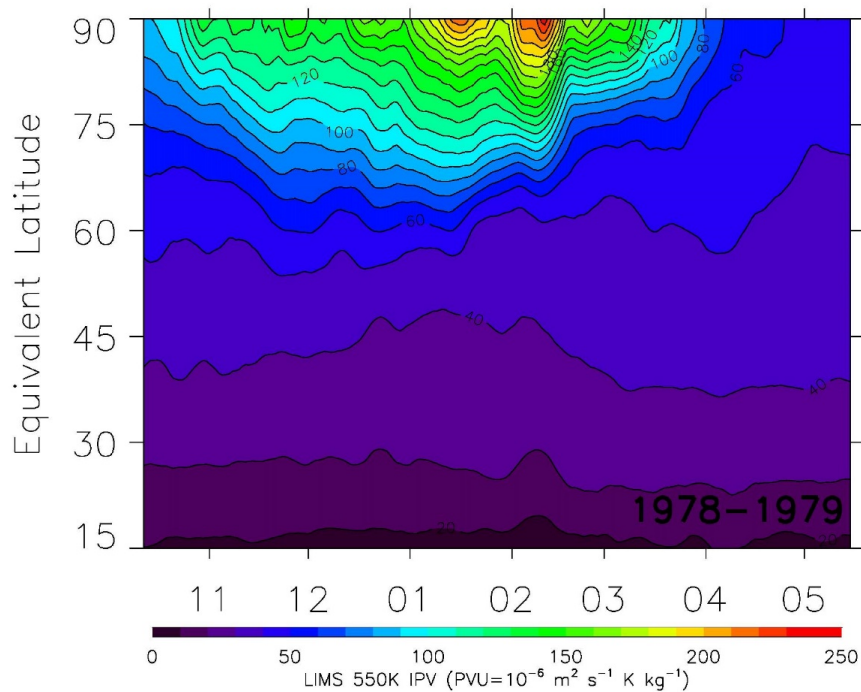
Figure 12. Time series of LIMS isentropic PV versus equivalent latitude at 550 K and with

smoothing over 7 days. PV contour interval (CI) is 10 units.

793

794

795
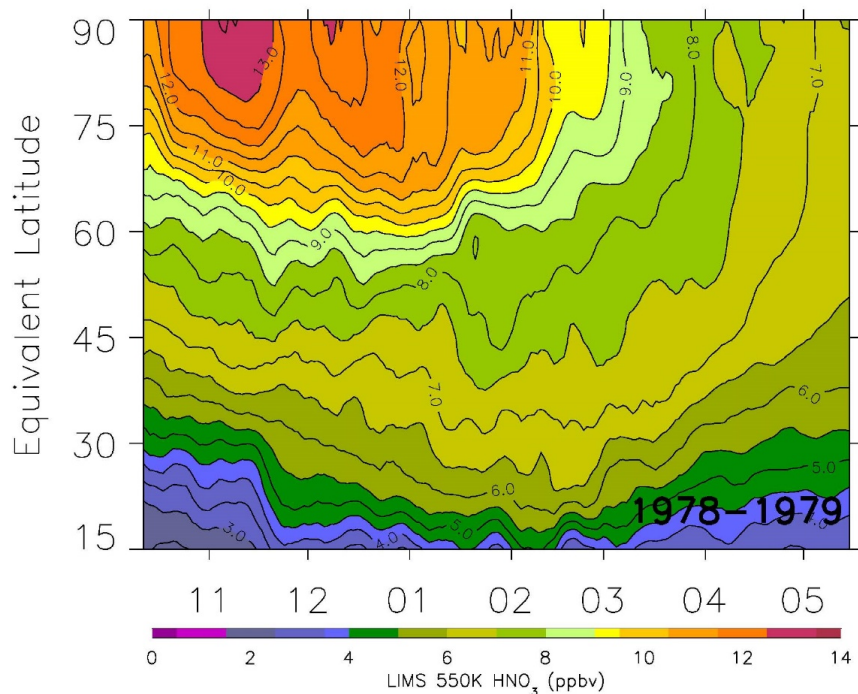
Figure 13. As in Fig. 12, but the averages of HNO_3 along PV isolines (CI is 0.5 ppbv).

797

798

799
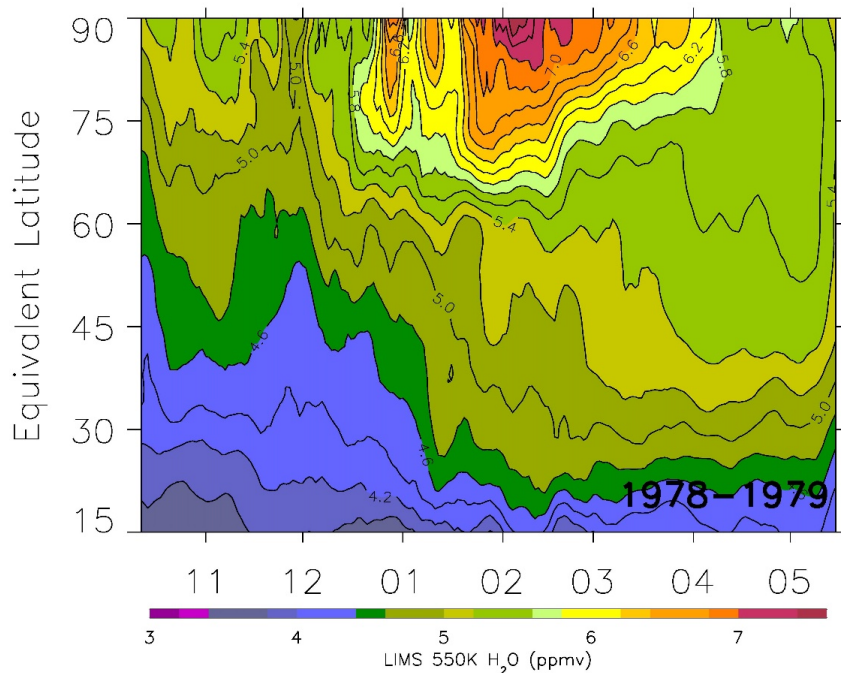
Figure 14. As in Fig. 13, but as averages of H_2O (CI = 0.2 ppmv).

801

802
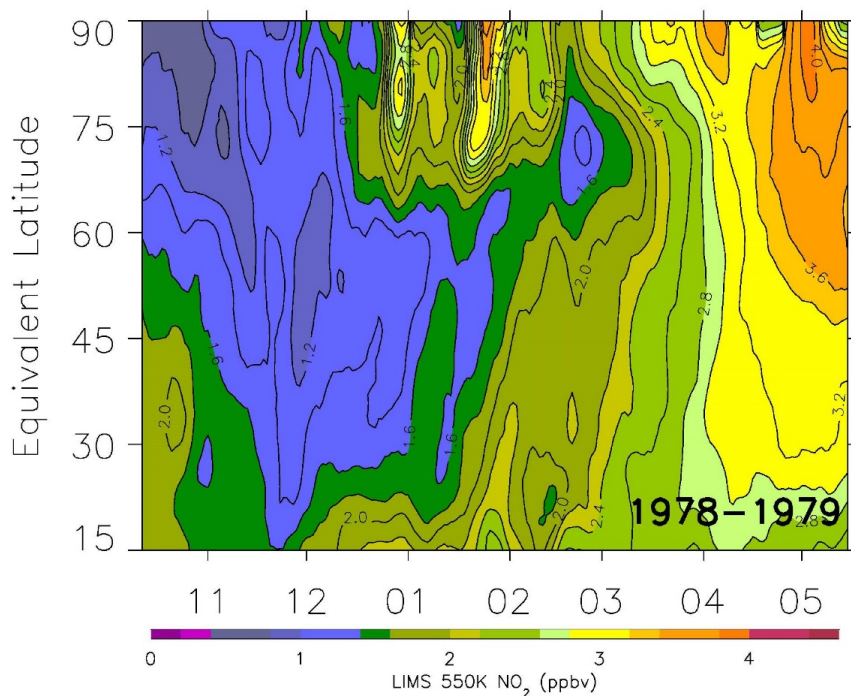
803

804 **Figure 15.** As in Fig. 13, but as averages of descending orbital (nighttime) NO_2 (CI = 0.2 ppbv).

805